# Underbody flow control for base drag reduction of a real car model

Laurent Keirsbulck, Olivier Cadot, Marc Lippert, David Boussemart, Jérémy Basley, Sébastien Delprat, Sébastien Paganelli

# Underbody flow control for base drag reduction of a real car model

Laurent Keirsbulck[b,c], Olivier Cadot[a], Marc Lippert[b,c], David Boussemart[b,c], Jérémy Basley[b,c,*], Sébastien Delprat[b,c], Sébastien Paganelli[b,c]

[a] *School of Engineering, University of Liverpool, Liverpool L69 3GH, UK.*
[b] *Univ. Polytechnique Hauts-de-France, UMR 8201-LAMIH-, F-59313 Valenciennes, France.*
[c] *CNRS UMR 8201, F-59313 Valenciennes, France.*

**Abstract**

A 1:5 scale realistic car model of the original Twingo GT but presenting a flat underbody and no exhaust line is tested in a wind tunnel at Reynolds numbers $Re = 2.15 \times 10^5$ to $4.3 \times 10^5$. A range of underbody flow characteristic velocities $U_b = [0.5 - 0.72]\, U_\infty$ ($U_\infty$ the free-stream velocity) is obtained by two techniques: flow obstruction and low momentum injection. Force balance, pressure measurements and Particle Image Velocimetry are used to characterize the aerodynamics of the model while changing the underbody flow velocity. A very sharp transition in the wake is found at a critical underbody velocity $U_b = 0.65U_\infty$. It corresponds to a sudden wake reversal with a bistable behavior between 2 equilibrium states, N or P depending on the vertical base pressure gradient or the wake orientation. The drag of the N state is larger than that of the P state. The control of the wake state by reducing the underbody flow velocity leads to beneficial increase of the base suction of approximately 20% when selecting the P state compared to the N state. The low momentum injection technique reduces drag by 10% but is ineffective at yaws 5° and 10°, while the obstruction technique consistently increases base suction but induces additional drag.

## 1. Introduction

The passenger car industry has shown increasing interest in underbody flow to improve the aerodynamic performance of cars. The underbody structure that mainly consists of wheels arches, exhausts lines and cooling system is a source of drag (see for instance Yuan and Wang (2017)) due to the multiple flow separation it generates compared to a smooth plate. An important geometrical effect for drag reduction is the angle at rear separation (called the diffuser angle) that is able to increase the pressure at the base of the vehicle as shown in Cooper et al. (1998) of which applications can be found in Huminic and Huminic (2020); Buscariolo et al. (2021) for simplified geometries and in Guerrero et al. (2022) for a more realistic car model. For ground clearances (vertical distance between the underbody and the road) typically larger than 8% the body height (Cooper et al., 1998), the drag coefficient obtained with moving ground (the real on-road boundary condition) remains sensibly close to that with static ground. This general trend is consistent with the pressure distributions obtained around real cars by Carr (1975) in on-road condition and wind tunnels with static ground. Similarly, the CFD of Wang et al. (2019) on a generic commercial car model, with static or moving ground showed almost no difference in the wake. Hence it seems that the boundary layer that develops on the static ground below the underbody flow and behind the car has sufficiently small effect on passenger-car aerodynamics that wind tunnel testing with static ground is a relevant approach.

The sensitivity of the rear wake orientation of industrial minivans to the underbody flow has been evidenced with variations of axle clearances (vertical gaps between the road and the underbody at the front and rear axles) and closure of the front air intake by Bonnavion et al. (2019). The front air intake system impacts the underbody flow because the incoming air flowing through the engine parts to be cooled is evacuated with very low momentum in the car underbody. The closure of the front air intake increases the underbody flow velocity as would an increase of the clearance. Bonnavion et al. (2019) investigated 4 real different models with rotating wheels and road effect in a full scale wind tunnel; namely the Peugeot 5008, Peugeot Partner, Citroën Berlingo and Renault Kangoo. They found

*Corresponding author
*Email address:* jeremy.basley@uphf.fr (Jérémy Basley)

that large clearances or closed air intake are associated with a negative vertical (perpendicular to the ground) component of the base pressure gradient (called N state of the wake) while small clearance or open air intake are associated with a positive vertical component of the base pressure gradient (called P state of the wake). The rear wake orientation correspond to a flow deviation towards the same direction of the base pressure gradient. The transition between the P and N state is not continuous but discrete where the mean gradient jumps between the two distinct values of the P and N state involving random bistable dynamics. These wake states can be recovered with simplified geometries having a taller than wide rectangular base and a static ground. Grandemange et al. (2013) was the first to evidence vertical states on a Ahmed-type model (Ahmed, 1983), referred to as the $z$-instability because of the $z$-direction perpendicular to the ground of the vertical base pressure gradients. Later, Schmidt et al. (2018) confirmed the presence of vertical P and N states in the rear wake of a General European Transport System, a simplified geometry to mimic a heavy-duty vehicle. The first and so far the only numerical simulation to report wake states in the vertical direction is due to Dalla Longa et al. (2019). Recently, Fan et al. (2022) found, for a taller than wide Ahmed-type model, discrete transitions between the vertical P and N states either induced by the pitch, the ground proximity and the yaw. Fan et al. (2024) investigated the states observation modifying the cross flow of the wake by means of body pitch and flow orientation using top and bottom tappers. Whatever the means used, an upwash increase is likely to reverse an N state into a P state, and conversely a downwash increase is likely to reverse a P state into an N state.

There are now strong evidences that the wake states observed for the industrial minivans and simplified ground vehicle models relate to a fundamental property of three-dimensional bluff-bodies presenting a wide recirculating region at their base. In the absence of a ground proximity, the recent theoretical work of Zampogna and Boujo (2023) shows that for a Reynolds number of few hundreds (the critical Reynolds number actually depends on the forebody geometry and body length), the recirculating flow at the base of a prism looses the symmetry of the geometry and encompasses a pitchfork bifurcation towards a deviated wake defining the steady global instability. The deviation occurs in the direction of the major axis of the rectangular base resulting in a permanent base pressure gradient in that same direction. There are two possible orientations having base pressure gradient of opposite signs, the so-called P and N states. Hence, the observation of the different wake states for industrial minivans and simplified geometries having a rectangular base presenting a vertical major axis (i.e.; taller than wide base) is very likely to be a persistence at large Reynolds number and with a ground proximity of the steady global instability revealed by Zampogna and Boujo (2023).

As a possible universal property of recirculating flow at the rear of three-dimensional bluff-bodies, the steady global instability should be shared by a large variety of industrial vehicles. Although it is rarely explicitly mentioned as an instability in the literature, global wake asymmetries in the vertical direction have been reported for realistic models by other authors. The full scale real SUV studied by Khalighi et al. (2012) displays a clear vertical asymmetry in agreement with a P state observable in the symmetry plane of the wake flow field and also in the base pressure distribution. Avadiar et al. (2018) conducted wind tunnel testing to characterize a DrivAer estate vehicle having a flat underbody surface. A wake vertical asymmetry consistent with a P state is also observable in their pressure distribution. The same DrivAer estate vehicle has been investigated with a CFD in Wang et al. (2019) to characterize the difference between a moving and static ground. Their conclusion confirms that the static ground configuration only locally alters the flow field in close proximity to the ground, and therefore its impact on the flow near the automobile surfaces and in the wake is limited. The P state of the wake remains observed in all cases. No bistability phenomena was reported in Khalighi et al. (2012); Avadiar et al. (2018); Wang et al. (2019) who considered only one flow configuration. It then seems that parametric studies involving variable body attitude and air intake such as those investigated in Bonnavion et al. (2019) are necessary to evidence bi-stable dynamics.

Due to the absence of symmetry in the vertical direction (related to the ground proximity and model shape), there is no reason for the drag of both P and N wake states to be identical. The relative difference during the bi-stable dynamics has been reported to be about 3% for the industrial minivans (Bonnavion et al., 2019) and the simplified geometry (Fan et al., 2022), although the state which minimizes the drag is not the same. Bonnavion et al. (2019) found that the wake P state has the lowest drag for minivans, while Fan et al. (2022) reported the wake N state to have the lowest drag for the simplified geometry. This apparent contradiction might be explained by the difference in lift coefficients, that is positive for minivans and negative for the simplified body. It is

then likely that the low drag wake having a vertical base pressure gradient of the same sign as the lift coefficient always contributes to the lift in such a way to reduce its magnitude. The part of the drag induced by the mean lift (Howell, 2015) might thus be reduced (resp. increased) by the low (resp. large) drag wake state for both the real minivans and the simplified geometry.

The ideas of the present work is $(i)$ to show that in addition to the car models cited above, the rear wake of a popular car geometry (a Renault Twingo model) presents the global steady instability, thus highlighting the importance of this fundamental property for industrial aerodynamics and $(ii)$ to use the known sensitivity of the states orientation to the underbody velocity to control wake and drag. This control technique of the recirculating region, likely independent to the geometrical detail of the body might have a potential of a wide range of application. Technically the first manipulation technique, related to the air cooling system of real cars, is to inject low momentum in the underbody with steady jets of adjustable flow rate. The second technique is to create a flow obstruction in the underbody. Eventually, the base pressure gradient dynamics obtained during the wind tunnel testing manipulating the underbody flow is compared to real environment data. The article is organized as follows. The experimental setup is detailed in Sect.**2**. Next, Sect.**3** is devoted to the presentation and discussion of the results that are concluded in Sect.**4**.

## 2. Experimental configuration

This section describes the experimental setup including the real car model arrangement in the wind tunnel and the different measurement techniques used. In addition, we expose details on the underbody devices used to perturb the vertical wake equilibrium.

### *2.1. Wind-tunnel facility and instrumented car model*

The present experiment is performed in a closed-loop subsonic wind-tunnel with a 6.25:1 contraction ratio. The 10m-long working section has a $2 \times 2\text{m}^2$ cross-sectional area and the free-stream turbulent intensity is less than 0.6%. The real car model shown in Fig.1a is a Renault Twingo GT. The model is centred between the side walls, the ceiling, and the floor within the test section and placed in wall proximity with a plate up raised above the floor within the test section. The coordinate system is defined as (**x**,**y**,**z**) in the streamwise, spanwise, wall-normal directions, respectively, as shown in Fig.1a and Fig.1b. The real car model has a width, $w$ of 297mm and a height, $h$ of 215mm, leading to an aspect ratio, $w/h$ of 1.38, and a length, $L$ of 653mm, the four square supports connected to the wheels have a side length of 15mm. The ground clearance, is set to $c = 44$mm and the body have a frontal area of 0.0765 $m^2$. The model corresponds to the original real Twingo GT configuration with a scale of 1:5 without exhaust line and underbody real geometry. In the present case, the underbody has a flat surface. The blockage ratio, defined as the ratio of the projected area of the model (including the model support) in the direction of incoming flow to the cross-sectional area of the wind tunnel test section is of 4.3%.

### *2.2. Force, pressure and velocity measurements*

The total drag and side force coefficients $C_D$ and $C_y$, respectively, are defined by $C_D = F_x/(S.q_\infty)$, and $C_y = F_y/(S.q_\infty)$, where $F_x$ and $F_y$ are the measured drag and side forces, $q_\infty = \frac{1}{2}\rho U_\infty^2$, with $\rho$ the air density, and $S$ the projected frontal body area. In order to quantify the total aerodynamic drag and side forces, a 6-components Delta Ati balance (Mc-3a model 100) with a sensitivity of $5.4\mu$V/VN and a capacity of 220N is used. A Dewesoft signal conditioner processes the raw sensor measurements with a resulting resolution estimated to $\pm$0.01N. Force measurements are low-pass filtered using a zero-phase digital filter in order to reduce noise and preserve the temporality of the signals.

The pressure is measured at 63 locations on a $9 \times 7$ grid at the back of the body as shown in Fig.1c. The pressure taps are equally spaced with distances $\delta y^* = 0.102$ in the **y**-direction and $\delta z^* = 0.093$ in the **z**-direction. The instantaneous pressure coefficient is computed by:

$$c_p(t) = \frac{p(t) - p_\infty}{q_\infty}$$

with $q_\infty = \frac{1}{2}\rho U_\infty^2$ and where $\rho$ denotes the air density, and $p_\infty$ the reference static pressure, measured at the side-wall of the test section, aligned with the front of the body. The base suction coefficient $c_b$ is computed from the spatial average of the 63 pressure taps at the base:

$$c_b(t) = -\frac{1}{63}\sum_{i=1}^{9}\sum_{j=1}^{7} c_p(y_i, z_j, t)$$

The base suction coefficient represents the contribution of the body base to the total drag coefficient.

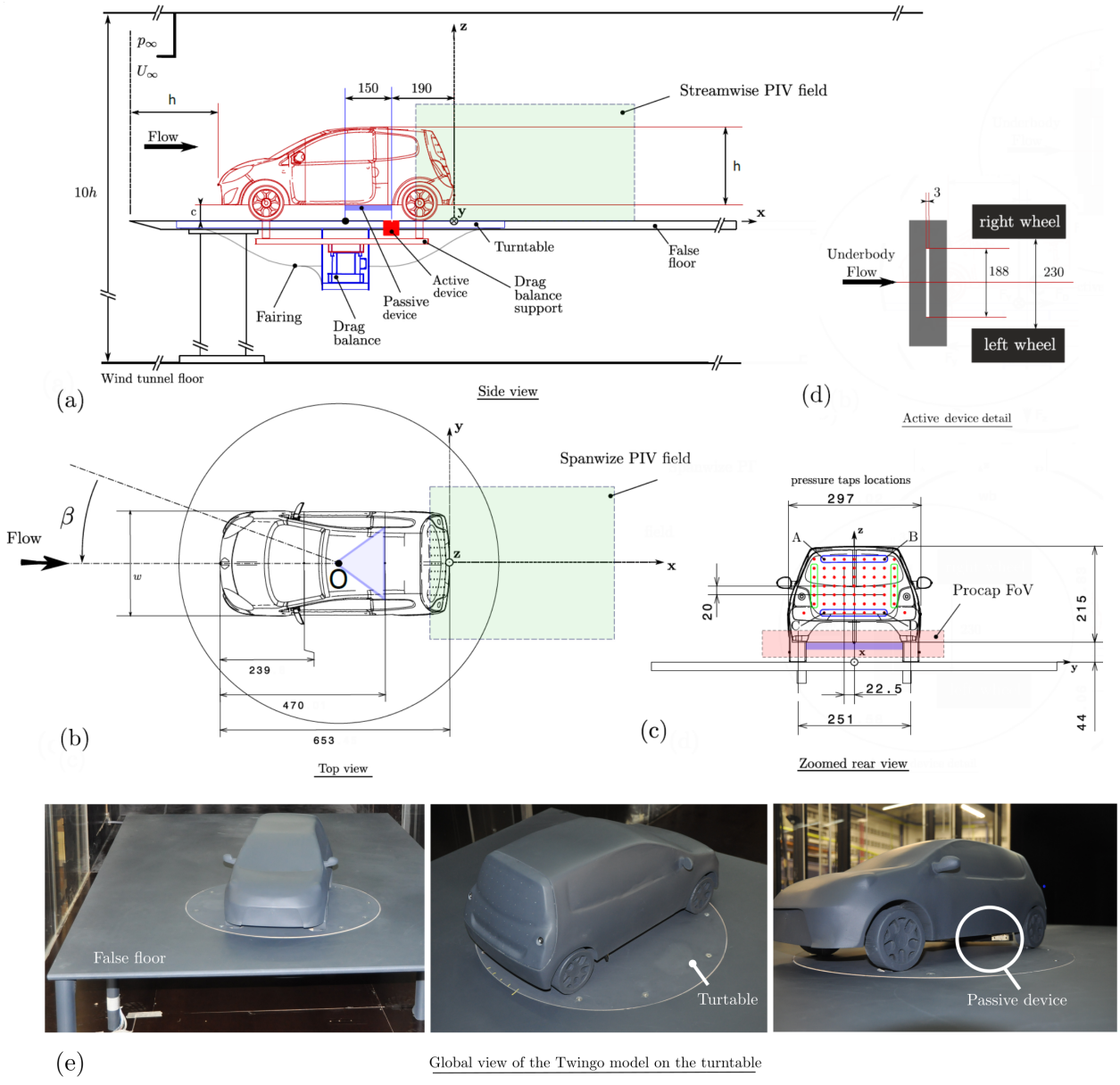


Figure 1: Experimental set-up. (a) Arrangement of the car model inside the test section including the control devices location and the PIV field of view (FoV), (b) Top view of the yawed arrangement with the fixed spanwise PIV FoV, (c) Time-resolved pressure location on the base, (d) Detail of the active control device. (e) Illustrations (several views) of the Twingo model placed on the turntable with the passive control system. All dimensions are in mm

As reported in Roshko (1993), it is a fundamental characteristic for bluff body flows that is sensitive to the rear wake dynamics. The temporal mean and standard deviation are denoted $C_p$ and $C'_p$, $C_b$ and $C'_b$ for the pressure and base suction coefficients respectively. The pressure scanner is located inside the model so that it is linked to each tap with less than 150mm of vinyl tube to limit the filtering effect of the tubing, leading to a natural low pass filtering of cutoff frequency approximately equal to 150Hz ($f_c^* = 1.41$). The accuracy of the pressure scanner (effective measurement range of 2000 Pa) is given by the manufacturer to be $\pm 0.15\%$ of the measurement range corresponding to $\pm 3$ Pa. However, converged time averaged values have a better accuracy that falls below $\pm 0.5$ Pa. So the accuracy in terms of mean base suction coefficients is $\pm 0.001$. The 63 pressure channels are recorded during 30s for each jet cases and during 300s for the cases with the passive triangle device (TR) at a sampling frequency of 850Hz per channel. The wake asymmetry is assessed by using the dimensionless horizontal and vertical base pressure gradients, $g_y$ and $g_z$. The four pressure taps group (**L**, **R**, **T**, **B**) indicated in blue and green in Fig.1c are used to compute the base pressure gradient components:

$$g_y = \frac{\langle c_p \rangle_{\mathbf{R}} - \langle c_p \rangle_{\mathbf{L}}}{8\delta y^*}, \quad g_z = \frac{\langle c_p \rangle_{\mathbf{T}} - \langle c_p \rangle_{\mathbf{B}}}{6\delta z^*}$$

with $\langle . \rangle_n$ denotes the spatial average of the taps group $n$. For the comparison with on-road real car testing (appendix), only points **A**, **B**, **C** and **D** locations (see Fig.1c) are used for the calculation of the gradients components to have same pressure taps location in both cases (model and full scale). The temporal mean and standard deviation of both gradient components $i = y, z$ are denoted $G_i$ and $G'_i$ respectively.

In the paper, we adopt the following notation : the superscript $^*$ denotes the non-dimensional value by using $h$, $U_\infty$. Instantaneous quantities are denoted with lower case letters , their temporal mean with upper-case letters , and their standard deviation with primed upper-case letters . Also, P and N stand for the positive and negative states of the vertical pressure gradient $g_z$.

The Particle Image Velocimetry (PIV) measurements are carried out with a standard two-component TSI system, composed of a double-pulse 200mJ dual-head Nd-Yag (Quantel Bslt220) laser system and two high-resolution CCD Powerview cameras with a full resolution of $2048 \times 2048$ pixels and micro Nikkor 50mm optical lens. The seeder is a TSI oil droplet atomizer 9307 whose droplets diameter's main mode is about $d_p = 1\mu$m. The seeding is released in the settling chamber of the wind tunnel. The vector fields are obtained by processing the PIV images using a recursive cross-correlation algorithm with a final interrogation window size of $16 \times 16$ pixels with 50% overlap. The resulting PIV fields of view passing through the streamwise and the spanwise middle planes of the car model as mentioned in Fig.1 are about $310mm \times 280mm$ (i.e. $1.44h \times 1.30h$) and $250mm \times 360mm$ ($1.16h \times 1.67h$) respectively. For every test case, 2000 time-uncorrelated PIV snapshots are recorded with a repetition rate of 7Hz. The maximum uncertainty on the instantaneous velocity fields considering an absolute displacement error of 0.1 pixels is estimated to be less than $0.01U_\infty$.

The complex three-dimensional active control jet and underbody flows behind the car model (pink areas on Fig.1 named Procap FoV) are measured with the probe Capture anemometry (ProCap system) consisting of a hand-guided 5-hole pressure probe, whose instantaneous position is tracked in real time by a motion capture camera system. The location of the probe is obtained by the infrared cameras through reflective passive markers on the probe. The tracking rate of 200 Hz ensures that each measurement point can be attributed to a position in the volume of interest. All three velocity components, static and dynamic pressure are measured with a five-hole probe and interpolated onto a regular grid and presented on a screen in real time. For the presented measurement a spatial resolution of 5mm was chosen with a total measurement time for a full area of interest scan at this resolution is at the order of 10 minutes. The data are post-processed using both ParaView and Matlab. Based on the height of the model, the Reynolds number of this flow is defined as $Re = U_\infty h/\nu$, where $\nu$ is the kinematic viscosity of the air at ambient temperature and $U_\infty$ the free-stream velocity. Experiments are conducted at three different free-stream velocities, $U_\infty$ of 15m/s, 20m/s and 30m/s leading to Reynolds numbers varying from $Re = 2.15 \times 10^5$ to $4.30 \times 10^5$.

### *2.3. Control devices*

The car clearance can be independently equipped with two kind of actuators; a passive device having the shape of an isosceles triangle obstructing one third of the ground clearance height (see Fig.1a,b). This passive control device is named TR in the following; an active device based on a flush mounted air knife blowers controlled by a proportional flow rate solenoid valve (flow control-Vef212 model), as

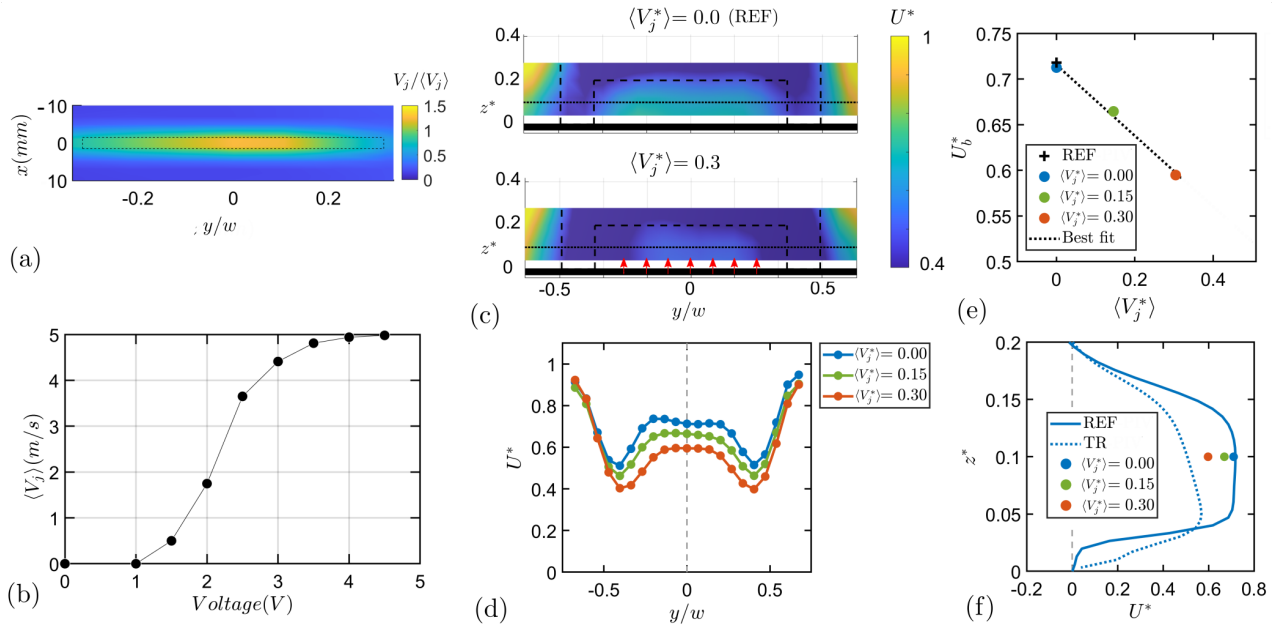


Figure 2: Underbody flow characterisation with and without controls. (a) Mean wall normal velocity field at the plan $z = 5mm$ above the blowing slit for a valve power supply voltage of $2.5V$. (b) Calibration of the power supply voltage with the jet velocity coefficient. (c) Mean streamwise velocity field at $x^* = 0$ (underbody exit) for the baseline (top) and for $\langle V_j^*\rangle = 0.3$ (bottom). (d) Mean streamwise velocity profiles at $z/c = 0.5$ for jet velocity coefficients $\langle V_j^*\rangle = 0, 0.15, 0.3$. (e) Characteristic underbody flow bulk velocity, $U_b^*$ vs. the jet velocity, $\langle V_j^*\rangle$. (f) Streamwise velocity profile along the wall normal direction in the mid-plane of the model for the baseline (REF) and for the passive device TR superimposed to the characteristic underbody velocity $U_b^*$ obtained from (d).

illustrated in FIG.1d and wall blowing actuator, hereafter named WBA. The slit width is $w_s = 3$mm and the actuation length is $l_s = 188$mm. The active device can generate different flow rate $Q$ related to the mean jet velocity $\langle V_j\rangle = Q/(w_s l_s)$. Technically, the ProCap is used to calibrate the valve power supply voltage on $\langle V_j\rangle$ when the wind tunnel is switched-off and the car model removed. FIG.2a shows the mean wall normal velocity distribution at the plan $z = 5mm$ given by the ProCap, of which its integration provides the value $\langle V_j\rangle$. The velocity distribution is almost centred to the middle plan of the setup with a velocity attenuation observed as one approaches the lateral extremities of the injection slot. The similar trend is observed for all the different supply voltages. The evolution of the mean jet velocity, $\langle V_j\rangle$ is plotted against the solenoid valve voltage supply in FIG.2b and reaches a maximum value of 5 m/s. The nonlinear behaviour is attributed to the electronic control system itself, but perfectly reproducible and repeatable.

The WBA control parameter is defined as the velocity coefficient $\langle V_j^*\rangle$, it ranges from 0 to 0.3 for the overall Reynolds number studied. The velocity coefficient can be converted into a flow rate coefficient $C_Q = \frac{\langle V_j\rangle w_s l_s}{U_\infty wc} = 0.043\langle V_j^*\rangle$, where the injected flow rate is compared to a reference underbody flow rate. Accordingly to the velocity coefficient range, we have $0 < C_Q < 0.013$ in this study.

## 3. Results

Results are organized as follows. First, the underbody flow is characterized in §3.1 for both passive device (TR) and active wall blowing actuator system (WBA). The effects of the wall blowing actuator and the passive device contributing to the suction and drag coefficients are evidenced in §3.2. Wake reversals between the P and N state and their bistable dynamics are then investigated varying the underbody bulk velocity in §3.3. A detailed analysis of the demonstrative passive manipulations of the wake state selection is investigated to prove its significance. Their aerodynamic impact is compared in terms of robustness with the blowing actuator wake flow response in §3.4 varying yaw angle. Finally, wake dynamics obtained from on-road testing described in the appendix are compared to the wind tunnel testing in §3.5 to open perspectives for real application.

### 3.1. Underbody flow characterization

The velocity field at the underbody exit is investigated to determine the influence of the two control devices and to provide a characteristic underbody flow velocity $U_b$.

For the active device WBA, it is achieved by extracting the mean streamwise velocity field at the plane $x^* = 0$ from the ProCap 3D-measurements (see ProCap FoV in FIG.1c). FIG.2c(top) shows the streamwise velocity for the baseline (REF) where a typical velocity of $U^* \approx 0.7$ can be observed at the central part. The blowing case at a velocity $\langle V_j^* \rangle = 0.3$ (lower than the typical underbody flow) in FIG.2c(bottom) clearly lowers the underbody flow to $U^* \approx 0.6$. We define the characteristic velocity $U_b^*$ as the velocity at mid clearance ($z/c = 0.5$ or equivalently $z^* = 0.1$) and on the symmetry plane $y^* = 0$. FIG.2d illustrates the definition of $U_b^*$ from the horizontal velocity profile at $z/c = 0.5$ obtained for 3 blowing cases. It can be seen that $U_b^*$ is representative of the largest velocity at the underbody exit corresponding to a plateau value in between the wheels. The relation between the jet velocity coefficient $\langle V_j^* \rangle$ and the characteristic underbody velocity $U_b^*$ is shown in FIG.2f. This relationship is used together with that of FIG.2b to convert the voltage of the valve power supply into the characteristic velocity $U_b^*$ of all experiments using the active device WBA in the following.

The PIV system has been used to characterize the underbody flow with the passive device TR. The streamwise velocity profile at mid-plane of the underbody exit ($x^* = 0, y^* = 0$) is shown in FIG.2f without and with the device. Compared to the values $U_b^*$ obtained during the WBA experiments, there is a good match between the two cases with no control (REF and $\langle V_j^* \rangle = 0$), while the case with the TR device achieves the smallest underbody flow of all controlled cases.

### 3.2. Wake states identification

The global contribution of the active and the passive devices to the suction coefficient $C_b$ as a function of the characteristic velocity $U_b^*$ is evidenced in FIG.3(top) for the three studied Reynolds numbers. There is a strong variation around a critical underbody velocity of $U_{b_c}^* \approx 0.635$, where the suction coefficient drops from 0.26 to 0.22 as the underbody flow decreases. It corresponds to a base suction reduction of about 15%. The 3 TR cases having the smallest underbody flow velocity also drop by similar amplitudes from the REF values. This transition seems to occur whatever is the Reynolds number and control

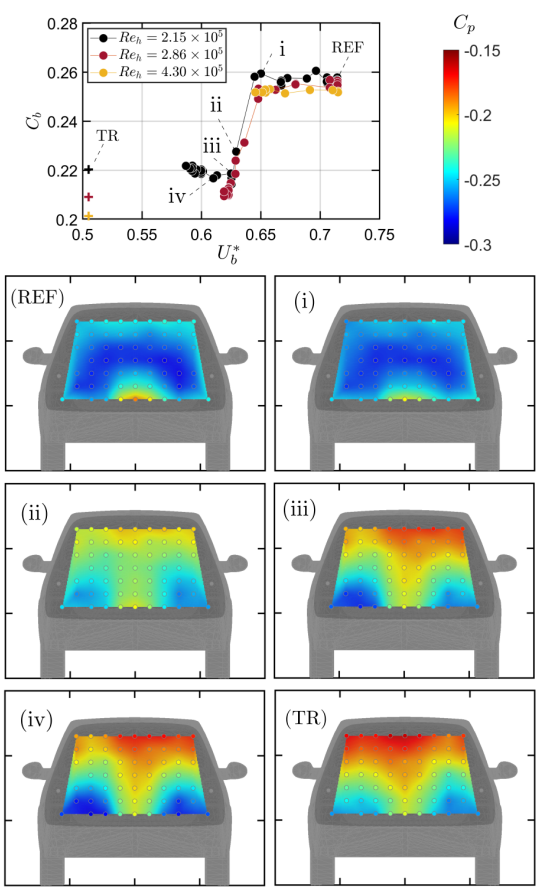


Figure 3: $C_b$ against $U_b^*$ for the three studied $Re_h$ and some associated map for $Re_h = 2.15 \times 10^5$ corresponding to different states from the baseline (REF), around the transition (from (i) to (iv)) and with the passive device (TR). Colored + symbols refer to the TR cases.

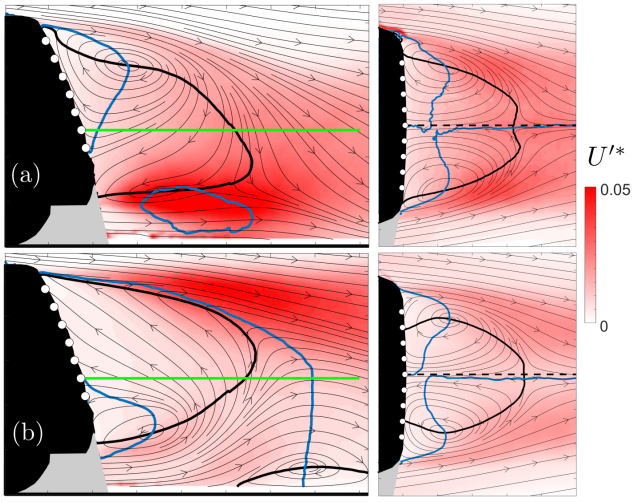


Figure 4: Characteristic wake reversal based on particle image velocimetry (PIV) field of view (FoV) in the vertical midplane (left side) and horizontal plane (right side and following the green line), (a) baseline (REF), (b) passive control device (TR). Black lines denote the iso-contour with a mean streamwise velocity equal to zero, blue lines the same for the normal velocity. Colormap refers to the streamwise component of the Reynolds stress at $Re_h = 2.15 \times 10^5$.

device type. To investigate the causes of this transition some points corresponding to different states from the baseline (REF), around the transition (from (i) to (iv)) and with the passive device (TR) are detailed in the second part of the FIG.3(bottom).

For the baseline (REF) and the case with $U_b^* > U_{b_c}^*$ (i.e.: case (i)), the mean pressure distribution at the base of the car shows a vertical negative gradient indicative of a vertical asymmetric state N of the wake. For these cases before the transition, the pressure distribution shows very small sensitivity to the underbody flow.

At the transition $U_b^* \approx U_{b_c}^*$ (i.e.: case (ii)), the pressure distribution changes drastically, noticeably with the appearance of a positive vertical gradient. After the transition, $U_b^* < U_{b_c}^*$ (i.e: cases (iii), (iv) and (TR)) there is almost no sensitivity of the pressure distribution to the underbody flow that exhibits now a clear positive vertical gradient indicative of a vertical asymmetric state P of the wake. The transition is thus associated with a vertical base pressure gradient reversal that is indeed induced by the wake reversal evidenced in FIG.4.

The wake flow topology associated with the state change is highlighted through the velocity fields on both sides of the transition, between the baseline shown in FIG.4(a) and the TR case in FIG.4(b). In both cases the mean wake has a planar symmetry with respect to the plane $y^* = 0$. The

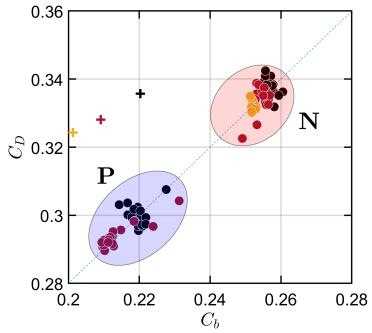


Figure 5: $C_D$ against $C_b$ for the three studied $Re_h$, with the TR passive device (+), and with the active wall blowing actuator (○).

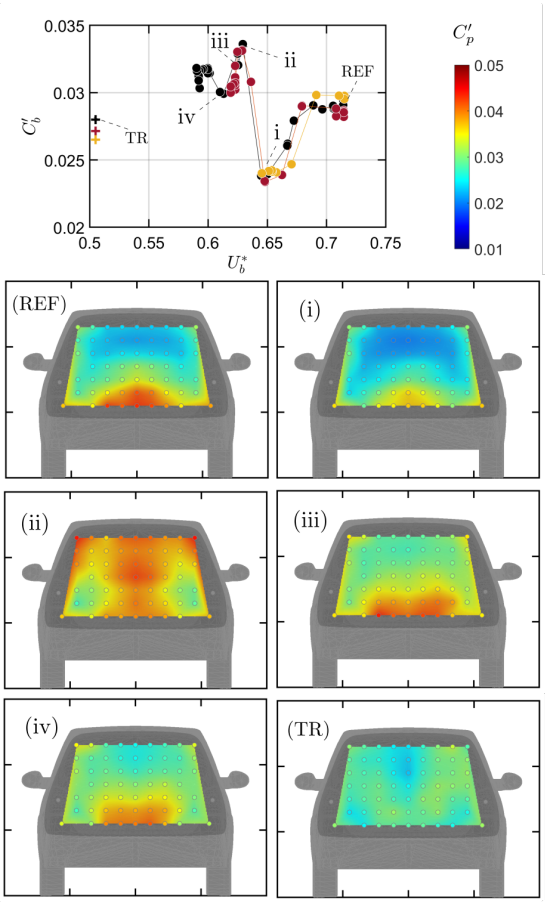


Figure 6: $C'_b$ against $U_b^*$ for the three studied $Re_h$ and for the various states of the FIG.3.

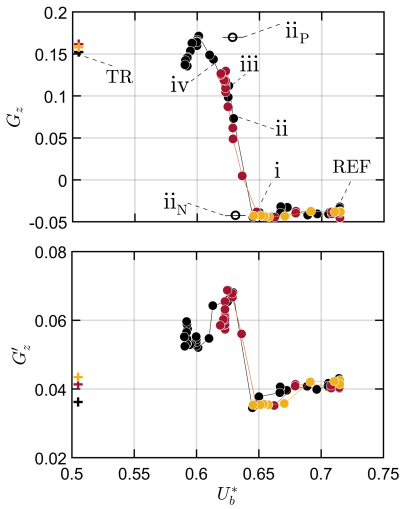


Figure 7: $G_z$ and $G'_z$ for various $U_b^*$ and for the three studied $Re_h$. Conditional states are given for the case (ii) on $G_z$ in order to capture the two states.

mean velocity field in the plane of symmetry displayed in FIG.4(b)(left)) shows a region with a closed streamlines on the side of lowest fluctuations $U'^*$ and a region of the impinging back flow on the side of the largest fluctuations $U'^*$. The vertical base pressure gradient evidenced in the distributions of FIG.3(REF) and FIG.3(TR) is orientated from the closed streamline region (low pressure) towards the impinging back-flow (high pressure). Thus FIG.4(a) indicates an N state and FIG.4(b)) a P state. The mean recirculating flow structure of the 2 wake states is similar to that reported for real minivans in Bonnavion et al. (2019) and also for simplified bodies with taller than wide rectangular base (Grandemange et al., 2013; Schmidt et al., 2018; Dalla Longa et al., 2019). The observed transition from the N state to the P state obtained by decreasing the underbody velocity in FIG.3 is equivalent to the states transition reported by Bonnavion et al. (2019) from closed to opened air intake of the Peugeot Partner with a moving ground and rotating wheels at a given attitude as shown in their Figure 16 (*a* & *d*).

As can be seen in FIG.4(b), the P state is associated with a flow separation on the floor marked with the zero iso-contour of the mean streamwise velocity. This separation is due to the dynamics of the boundary layer developing on the static ground and facing the adverse pressure gradient produced by the large car base suction (or the low base pressure coefficient). In the light of this observation, it is judicious to discuss the use of the static ground instead of a moving ground to address ground vehicle aerodynamics. In the work of Wang et al. (2019), the effect of the adverse pressure gradient produced by the DrivAer-Estate base suction is observable on the static ground. Although it does not produce a separation on the ground as in FIG.4(b)), it thickens significantly the boundary layer creating an upwash effect on the rear part of the recirculating region. The recent work of Fan et al. (2024) demonstrated for a simplified geometry that a wake in the N state requires additional upwash effect (or a positive vertical velocity) to produce a reversal towards the P state. It is then possible that the static ground indirectly contribute to the selection of the P state when $U_b^*$ is decreased in FIG.3 by the upwash effect produced by the boundary layer development due the low pressure at the base of the vehicle. However, since the N to P transition is triggered by the only closing/opening of the air intake of the Peugeot Partner in Bonnavion et al. (2019) with a moving ground (where flow separation on the ground is impossible because of the absence of a boundary layer), we are confident that the separation on the static ground is not the only mechanism to reverse an N state to a P state. The other mechanism would be simply the decrease of the underbody velocity as it is the case for the Peugeot Partner in Bonnavion et al. (2019). As we can't rule out a possible contribution of the static ground to the wake transition in our work, we believe that the critical underbody velocity $U_{b_c}^* \approx 0.635$ may be reduced with a moving ground.

The consequence on the drag can be seen in FIG.5 where the drag coefficient is plotted as a function of the base suction. For the WBA control, two clusters can be distinguished, the first is composed of states N and the second of states P, all of them seems to follow a trend $C_D = C_b + 0.08$ indicating that any gain on $C_b$ is equal to a gain on $C_D$. In other words, the drag reduction is uniquely due to the base suction change. The constant $C_0 = 0.08$ is likely to be the drag contribution of all parts of the car that is not the base. For the TR control, the drag coefficients are shifted towards larger values due to the drag contribution of the passive device such that now $C_0 = 0.12$.

The transition involves large pressure fluctuation as can be seen in the fluctuation $C'_b$ of the base suction as a function of the underbody velocity in FIG.6(top). Actually the highest fluctuations are obtained for the (ii) case where the base in FIG.6(ii) is covered at the top and bottom by large constant pressure fluctuations. For the case (i), fluctuations seem to decrease however the area of measurements does not cover the full base, and a high fluctuation region can be missed, thus biasing the result. The origin of the fluctuation at the transition is further

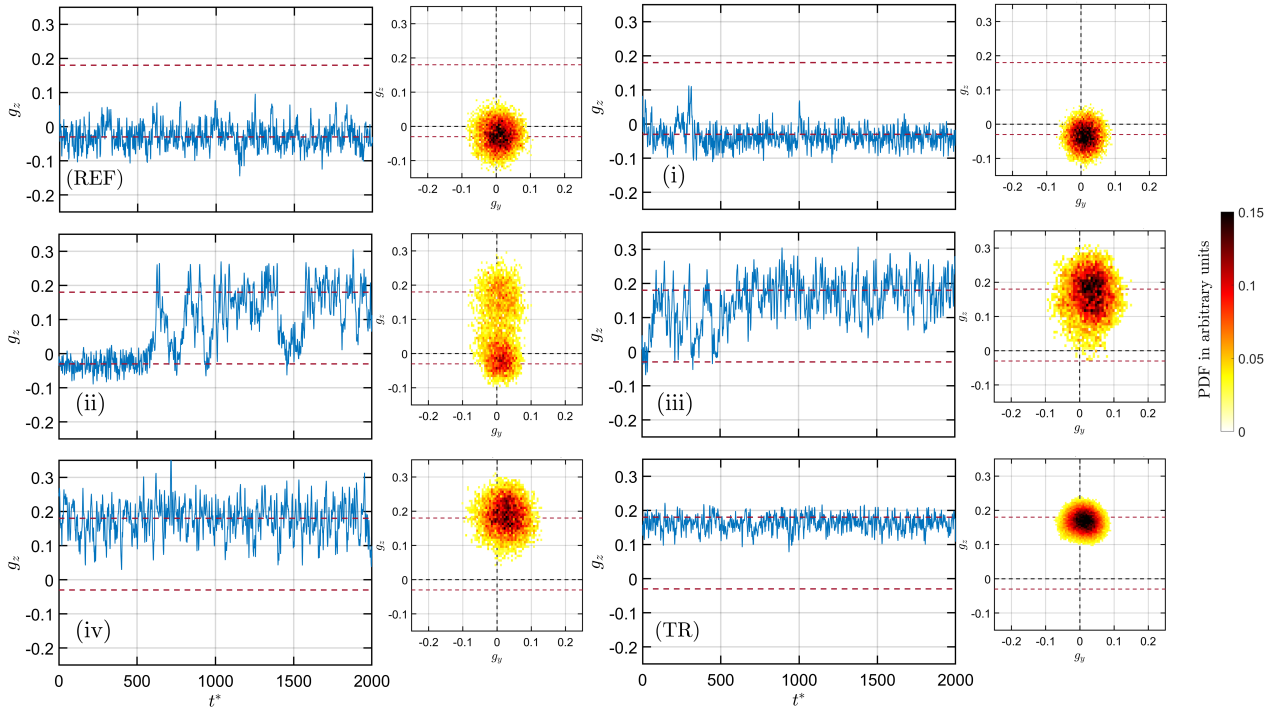


Figure 8: Time history of $g_z$ corresponding to the states of the FIG.7 with the associated PDFs of $g_y$ and $g_z$ at $Re_h = 2.15 \times 10^5$.

studied in the next section.

### *3.3. Bistable transition*

A focus on the wake dynamics and statistics is now addressed through the measurement of the base pressure gradients. FIG.7 shows the mean component of the vertical base pressure gradient $G_z$ and its fluctuation $G'_z$ as a function of $U_b^*$. Unsurprisingly, the mean vertical component switches from a negative value of approximately -0.05 to a positive value of approximately 0.15 with a crisis of fluctuation during the transition.

The global wake dynamics during the transition is illustrated in FIG.8 showing both the temporal evolution of the instantaneous vertical gradient $g_z$ and its joint PDF with $g_y$. For clarity, gradients are low pass filtered in the time history plots with a moving 50 ms window. This figure essentially shows that at the transition, the crisis of fluctuations in case (ii) is produced by bistable dynamics between the two wake states P and N. The value of the mean vertical gradient for each state, obtained by a simple conditionnal averaging, is reported in FIG.8 with labels $\text{ii}_\text{P}$ and $\text{ii}_\text{N}$. There is no doubt that this discrete transition is of same nature as in Bonnavion et al. (2019), thus revealing that the wake of the Renault Twingo GT is subjected to a steady instability responsible for the wake asymmetry in the vertical direction. An identical transition has been observed by Szmigiel (2017) in the wake of simplified boat-tailed truck model varying the underbody velocity by means of grids of different porosity. They observed a transition from the P to N state when the characteristic underbody velocity $U_b^*$ is increased from 0.4 to 0.85 with a sharp transition at 0.7 (see their Figure 5.6b). It is worth mentioning that the same model studied in Castelain et al. (2018) but with no boat-tailing (i.e.: square-back rear) only shows a clear P state until 0.85. It can be speculated that the transition to the N state for this rear geometry would have been observed with larger underbody velocity, produced for instance by a larger clearance as in Grandemange et al. (2013). In the present study, the critical underbody velocity for the transition ($U_{bc}^* \approx 0.635$) being significantly lower than 0.85 likely results from the velocity decrease induced by the top boat tail.

The transition between the two wake states generates notable changes in the dynamic activity of the unsteady global wake modes. FIG.9 shows the spectral content of the two pressure gradients $g_y$ and $g_z$ as well as the base suction coefficient for different cases: the reference case, TR and WBA with $U_b^* = 0.62$ (iv). The reference is in the N state while both TR and (iv) are in the P state.

The P state of the wake displays a similar spectrum whether it is achieved with the passive device or blowing as can be seen by comparing FIG.9(a) and FIG.9(b). In both cases, only a concentration of energy around $f^* = 0.2$ could be associated with a mode in the $g_y$ component corresponding to an antisymmetric horizontal mode likely to involve the lateral shears of the base separation. There is no clear concentration for the vertical component $g_z$ where instead, the energy spreads over a large domain expanding towards low frequencies. On the other hand, a clear concentration of energy is observed for $g_z$ around $f^* = 0.16$ for the N state of the reference wake in FIG.9(c) likely to be associated with a vertical antisymmetric mode involving the top and bottom shears of the base separation. For this N state, the horizontal mode at $f^* = 0.2$ is also identifiable in $g_y$, but with another concentration at $f^* = 0.035$. It is clear from these spectra that the P state and the N state are not a mirrored symmetry to each other (as suggested by the velocity fields in FIG.4), otherwise we would have expected identical spectra. Differences are thus related to all top/down asymmetries such as the trapezoidal shape of the base, the floor, wheels etc...

### *3.4. Yaw angle condition*

For the baseline case, yawing the body leads to an expected clear left/right asymmetry in the wake (FIG.10(a,b),) as well as in the base pressure distribution (FIG.10(e,f)) where the base pressure gradient becomes horizontal. The same trend at yaw is reported by Fan et al. (2022) for the simplified geometry where the horizontal component at the base has the same sign of the yaw angle. For the (TR) case that selects the P state of the wake at no yaw, it appears that the wake remains left/right symmetric until at least a yaw of 5° (FIG.10(c)) with still a dominant positive vertical base pressure gradient, indicating that the wake is still in a P state at 5° yaw, as can be seen in the corresponding pressure distribution in FIG.10(g). The left/right asymmetry becomes more obvious for a yaw of 10° in FIG.10(d,h). The values of the base pressure and the mean pressure gradient components are reported in FIG.11 at $\langle V_j^* \rangle = 0$ with black filled symbols for the baseline and empty symbols for the TR case. The larger base drag reduction is observed at 5°, and this is possibly a consequence to the wake that is kept in the P state (the low drag state as evidenced in the previous section) as seen in FIG.10(g).

The underbody blowing WBA case at yaw has almost no effect on the base drag in FIG.11(a). It

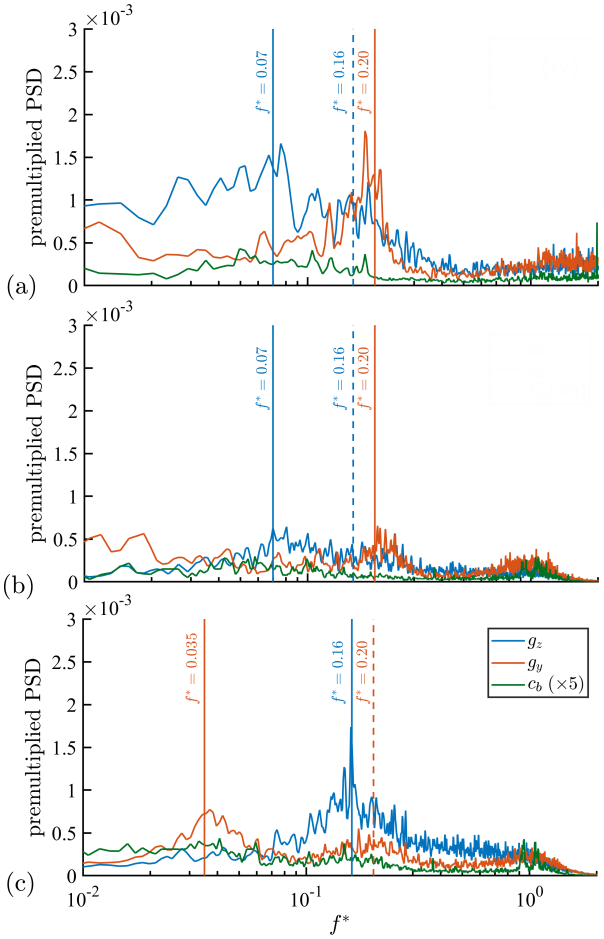


Figure 9: Premultiplied power spectrum densities of $g_z$, $g_y$ and $c_b$ for the WBA (iv) case in (a), the TR case in (b) and the baseline (REF) in (c) at $Re = 2.15 \times 10^5$.

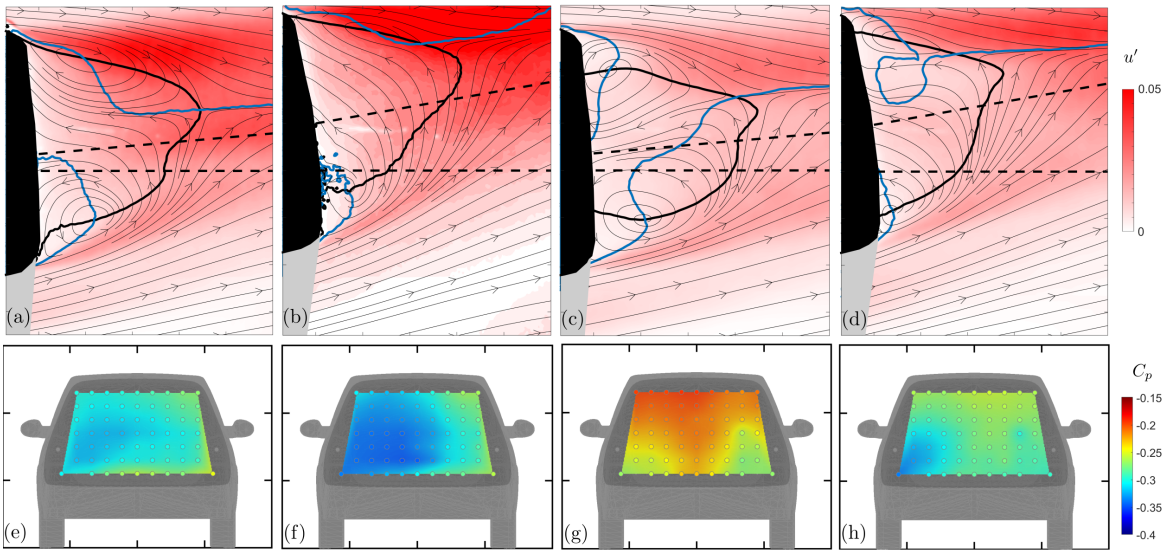


Figure 10: Yaw effect at 5° (a,e,c,g) and 10° (b,f,d,h) on the wake for the baseline (two first columns) and the TR cases (two last columns), (a) to (d) streamlines with the streamwise component of the Reynolds stress and (e) to (h), mean pressure coefficient distribution at $Re = 2.15 \times 10^5$.

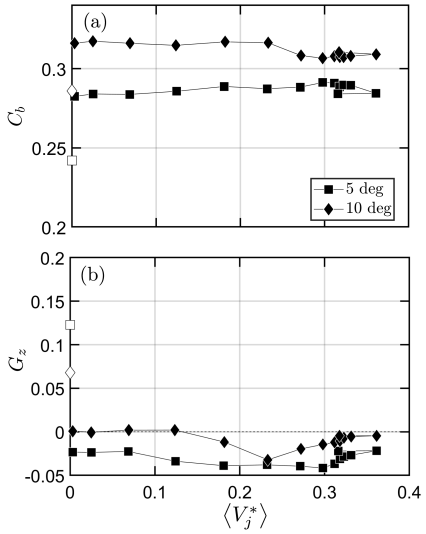


Figure 11: (a) Base suction coefficient $C_b$, (b) component $G_z$ of the mean base pressure gradient versus $\langle V_j^* \rangle$ for 5° and 10° yaw angles at $Re = 2.15 \times 10^5$ for the WBA (filled symbols). Open symbols denote the TR configuration.

seems that even for the lowest yaw 5°, the beneficial P state can't be triggered by the blowing. As a conclusion, drag reduction by underbody blowing is possible only if it is capable to produce a global effect of wake reversal, that is not achieved here for yaws at 5° and larger values.

To summarize, the wake of the real car model in the wind tunnel configuration is subjected to a global instability implying the possibility of 2 equilibrium states. The drag of the N state is found to be larger than that of the P state (as also found with real minivans wake in Bonnavion et al. (2019)). The control of the wake state by reducing the underbody flow with an active device leads to important drag reduction of approximately 10% when selecting the P state compared to the N state. The presence of the wake instability thus offers perspective for flow control and should be taken into account into industrial aerodynamics optimization. A first question is : what about the wake state in real driving situation ? We address the question with real environment testing on a gasoline Renault Twingo during a motorway trip (see appendix "On-road testing"). Equivalences with the wind tunnel experiment are actually not straightforward. With the difference in Reynolds numbers and the unsteady conditions related to the real environment, the additional complexity of rotating wheels, road effect, and the air intake system affect in a non-trivial way the underbody flow, making impossible to predict the wake state of the gasoline Renault Twingo from results

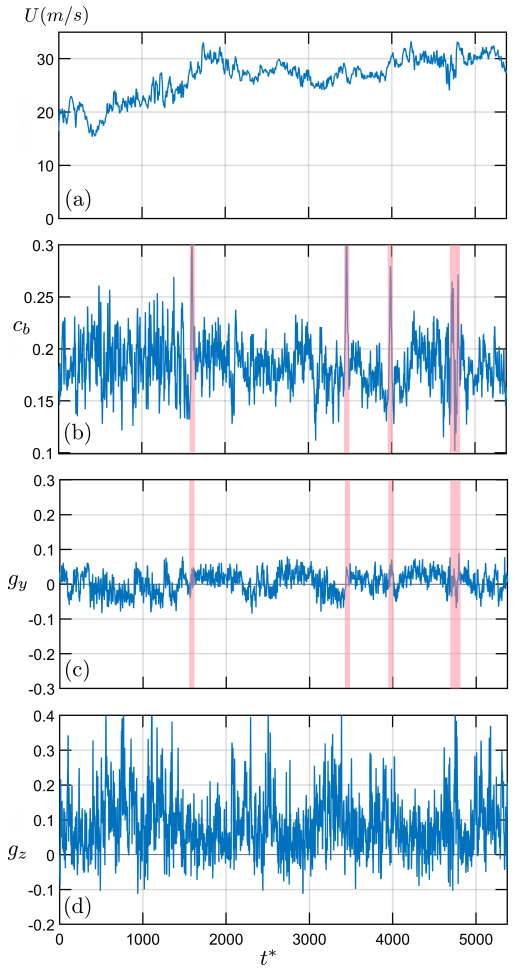


Figure 12: On-road time series, (a) vehicle velocity, (b) base suction coefficient, (c) horizontal $g_y$ and (d) vertical $g_z$ base pressure gradient. Pink bars denote overtaking events on the motorway.

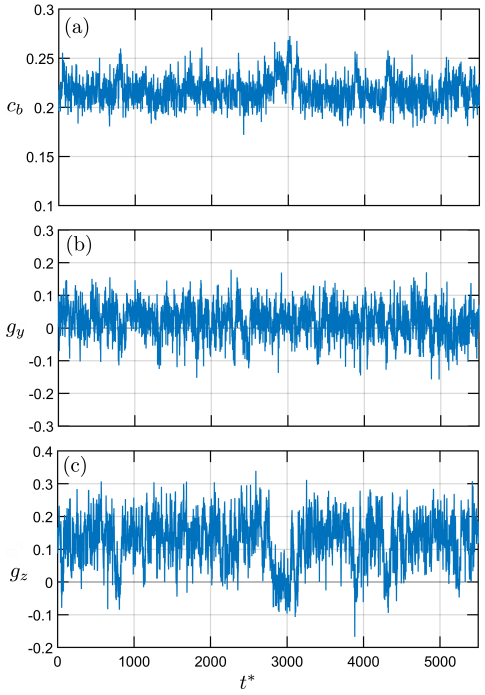


Figure 13: Active control time series (WBA) at $U_b^* = 0.62$, (a) base suction coefficient, (b) horizontal $g_y$ and (c) vertical $g_z$ base pressure gradient. For comparison with FIG.12, gradient components are recalculated from positions A,B,C and D (see appendix).

obtained in the wind tunnel in FIG.7.

### *3.5. Comparison with a real environment wake dynamics of the gasoline Renault Twingo*

The test has been carried out in real conditions as described in the appendix "On-road testing" and the main measurements are presented in FIG.12 with respect to the dimensionless time $t^*$. While FIG.12(a) gives the relative speed of the vehicle during the test, FIG12(b) depicts the base pressure coefficient highlighting the vehicle overtaking with pink areas. It can be seen that after the entry phase on the motorway at lower speed the pressure coefficient is fluctuating less and evolves around an average value of 0.19 with variations ranging from 0.22 to 0.1 and even 0.3 when overtaking occurred. Concerning the horizontal pressure gradient, represented in FIG.12(c), an evolution centered around zero with a relatively low amplitude around $\pm 0.05$ is systematically observed with sign changes that may correspond to environment modifications. For the vertical pressure gradient component, plotted in FIG.12(d), strong fluctuations are observed with a globally positive average value along the entire journey, highlighting a wake more likely to be associated with a P state.

In order to avoid any misleading interpretation, the gradient components obtained from the wind tunnel study above, are recalculated from pressure probes restricted to **A**, **B**, **C** and **D** positions as for the gasoline Twingo, and for the case (WBA) having the underbody flow characteristics $U_b^* = 0.62$ that also selects a state P of the wake (see FIG.13). Comparing the vertical gradient components of FIG.13(c) and FIG.12(d), clear differences remain between on-road and wind tunnel testing. While clear state switches are identifiable in FIG.12(d) (such as around $t^* = 3000$), the gradient fluctuates more homogeneously on a low frequency basis between 2 extreme values that could be ascribed to the P and N states. The correlation in the frequency domain between the base suction and the base pressure gradient components is obtained from the complex coherence function shown in FIG.14. Although the (WBA) case

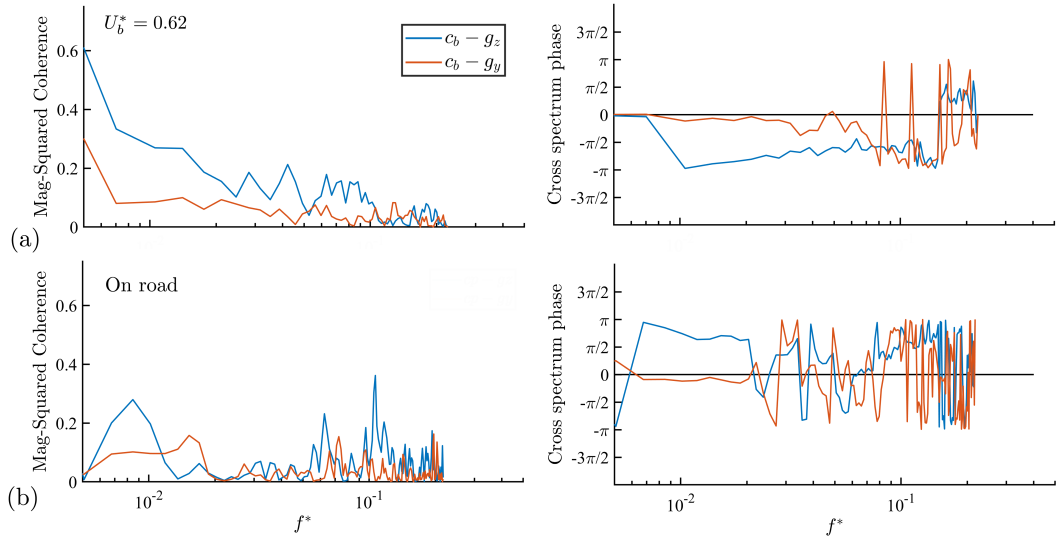


Figure 14: Magnitude squared coherence and cross spectrum phase between $c_b$ and the two gradient components, $g_y$ and $g_z$ for the (a) active control (WBA) at $U_b^* = 0.62$, (b) on road test. All are computed from the time series of Fig.12 and Fig.13.

presents a dominant P state of the wake, the few switches towards the N state are responsible for the evident correlation at low frequency between the vertical component $g_z$ and the base suction $c_b$ in Fig.14(a, left) with a $\pi$ shift in Fig.14(a, right). For the on-road testing, Fig.14(b) also indicates a similar correlation at low frequency, but much weaker than for the wind tunnel testing.

## 4. Conclusion

A car model corresponding to the original real Twingo GT configuration with a scale of 1:5 with an underbody flat surface and without exhaust line tested in a wind tunnel is subjected to a global instability implying the possibility of 2 equilibrium states, N or P depending on the value of the base pressure gradient. The drag of the N state is found to be larger than that of the P state (as also found with real minivans wake in Bonnavion et al. (2019)). The major contribution of the work is to show that the control of the wake state by reducing the underbody flow with an active device leads to important drag reduction of approximately 10% when selecting the P state compared to the N state. The transition occurs at a critical underbody velocity of $U_{b_c} \approx 0.635 U_\infty$. Based on the observation of a similar transition with moving ground (the correct ground boundary condition for vehicles), it is speculated that the static ground in the present experiment overestimates the critical velocity compared to moving ground. The very clear result is encouraging and may provide interesting perspective for flow control in real application. For this purpose, the base pressure gradient has been measured on a gasoline Twingo GT during an on-road testing. There are clear difficulties to compare both wind tunnel and on-road testing due to the large difference in underbody flows both vehicle may have. As the underbody flow characterisation is not accessible during the on-road testing, we have chosen to compare with the wind tunnel case having a similar state selection. A correlation between the vertical base pressure gradient and the base suction of same nature as that identified in the wind tunnel testing is still observable but much weaker. This latter result needs further development of on-road testing with on-board active control as real-life intermittent inflow conditions induce more complex dynamics, which are not captured in basic wind tunnel testing with uniform and low turbulent intensity flow.


## Acknowledgements

The present work (under the Ritmea research program) has been supported by the European Community, the Délégation Régionale à la Recherche et à la Technologie, the Ministère de l'Education Nationale, de la Recherche et de la Technologie, the Hauts-de-France région and the Centre National de la Recherche Scientifique. The authors gratefully acknowledge the support of these institutions.

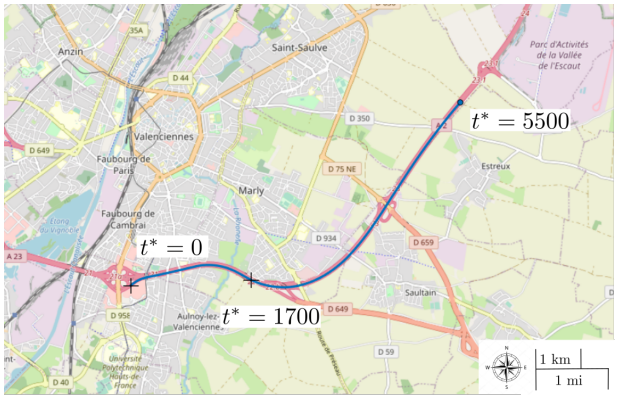


Figure 15: Motorway journey associated with the test sequence obtained using the on-board global positioning system.


Figure 16: Instrumented test vehicle

## Appendix. On-road testing

The sequence considered is a motorway journey (see FIG.15) with a departure with an acceleration phase corresponding to an entry on the motorway between $t^*$ =0 to 1700 followed by a phase at relatively constant speed with variations in environmental topology (line of trees, bridges, overtaking vehicles,...). A driver and an operator passenger are boarded in the front seats of the vehicle. The test vehicle used was a real Renault Twingo (as shown on FIG.16), with full scale dimensions including the exhaust line and the various underbody equipment leading to an overall lower ground clearance with non-constant upstream-downstream air flow depending on the underbody geometry. A set of pressure taps are installed at the vehicle rear surface only on specific location (**A**, **B**, **C** and **D** see FIG.1d) since it was not possible to drill directly all the part of the rear window. Nevertheless, the installed pressure taps are located to have the vertical and horizontal gradient at quite the same location of the four common positions (**A**, **B**, **C** and **D**) as it is the case for the wind tunnel model. As a consequence we do not have access to the full pressure map on the rear surface, so only an estimation of the pressure coefficient and the pressure gradient components are obtained base on these pressure taps. The tapping were connected to a pressure scanner (Scanivalve MPS4264) with 1 m of vinyl tube at a sampling frequency of 10 pressure samples per second. The power supplies are decoupled from that of the vehicle to avoid any interference problem or impedance matching. The dynamic pressure, $q_\infty$ and the reference pressure, $p_\infty$ were capture using a car front cover mounted standard Pitot-static probe as shown in FIG.16. The probe remained in position throughout the entire test run. This probe is not able to provide the instantaneous yaw angle data, and just measure the relative speed of the car. The pressure measurement were gathered in a synchronized way in order to be compute the pressure coefficient and the two pressure gradient components. The vehicle was driven at an indicated velocity between 20 to 30 m/s during the on-road test.

## References


Ahmed, S.R., 1983. Influence of Base Slant on the Wake Structure and Drag of Road Vehicles. J. Fluids Eng. 105, 429–434. doi:10.1115/1.3241024.

Avadiar, T., Thompson, M., Sheridan, J., Burton, D., 2018. Characterisation of the wake of the DrivAer estate vehicle. Journal of Wind Engineering and Industrial Aerodynamics 177, 242 – 259. doi:https://doi.org/10.1016/j.jweia.2018.04.013.

Bonnavion, G., Cadot, O., Herbert, V., Parpais, S., Vigneron, R., Délery, J., 2019. Asymmetry and global instability of real minivans' wake. Journal of Wind Engineering and Industrial Aerodynamics 184, 77–89.

Buscariolo, F.F., Assi, G.R., Sherwin, S.J., 2021. Computational study on an ahmed body equipped with simplified underbody diffuser. Journal of Wind Engineering and Industrial Aerodynamics 209, 104411.

Carr, G., 1975. Correlation of pressure measurements in model and full-scale wind tunnels and on the road. SAE Technical Paper 750065.

Castelain, T., Michard, M., Szmigiel, M., Chacaton, D., Juvé, D., 2018. Identification of flow classes in the wake of a simplified truck model depending on the underbody velocity. Journal of Wind Engineering and Industrial Aerodynamics 175, 352–363. doi:10.1016/j.jweia.2018.02.004.

Cooper, K.R., Bertenyi, T., Dutil, G., Syms, J., Sovran, G., 1998. The Aerodynamic Performance of Automotive Underbody Diffusers. SAE Transactions 107, 150–179. URL: https://www.jstor.org/stable/44740947. publisher: SAE International.

Dalla Longa, L., Evstafyeva, O., Morgans, A., 2019. Simulations of the bi-modal wake past three-dimensional blunt bluff bodies. Journal of Fluid Mechanics 866, 791–809.

Fan, Y., Parezanović, V., Cadot, O., 2022. Wake transitions

and steady z-instability of an ahmed body in varying flow conditions. Journal of Fluid Mechanics 942, A22.

Fan, Y., Parezanović, V., Fichera, S., Cadot, O., 2024. Towards adaptive drag reduction of a flat-back 3d bluff body in variable pitch and crosswind by flow orientation at the base separation. Experiments in Fluids 65.

Grandemange, M., Gohlke, M., Cadot, O., 2013. Bi-stability in the turbulent wake past parallelepiped bodies with various aspect ratios and wall effects. Physics of Fluids 25, 95–103.

Guerrero, A., Castilla, R., Eid, G., 2022. A Numerical Aerodynamic Analysis on the Effect of Rear Underbody Diffusers on Road Cars. Applied Sciences 12, 3763. URL: https://www.mdpi.com/2076-3417/12/8/3763, doi:10.3390/app12083763. number: 8 Publisher: Multidisciplinary Digital Publishing Institute.

Howell, J., 2015. Aerodynamic drag of passenger cars at yaw. SAE International Journal of Passenger Cars-Mechanical Systems 8, 306–316.

Huminic, A., Huminic, G., 2020. Aerodynamics of curved underbody diffusers using cfd. Journal of Wind Engineering and Industrial Aerodynamics 205.

Khalighi, B., Jindal, S., Iaccarino, G., 2012. Aerodynamic flow around a sport utility vehicle—computational and experimental investigation. Journal of Wind Engineering and Industrial Aerodynamics 107-108, 140–148.

Roshko, A., 1993. Perspectives on bluff body aerodynamics. Journal of Wind Engineering and Industrial Aerodynamics 49, 79–100.

Schmidt, H.J., Woszidlo, R., Nayeri, C.N., Paschereit, C.O., 2018. The effect of flow control on the wake dynamics of a rectangular bluff body in ground proximity. Exp. Fluids 59, 107.

Szmigiel, M., 2017. Etude du flux de soubassement sur la dynamique du sillage d'un corps non profilé à culot droit : Application du contrôle actif pour la réduction de traînée de véhicule industriel. Theses. Université de Lyon. URL: https://theses.hal.science/tel-02611982.

Wang, S., Avadiar, T., Thompson, M.C., Burton, D., 2019. Effect of moving ground on the aerodynamics of a generic automotive model: The driver-estate. Journal of Wind Engineering and Industrial Aerodynamics 195, 104000.

Yuan, Z., Wang, Y., 2017. Effect of underbody structure on aerodynamic drag and optimization. Journal of Measurement in Engineering 5.

Zampogna, G., Boujo, E., 2023. Linear and weakly nonlinear stability of rectangular prisms. J. Fluid Mech. 966, A19.